Title

Edge-Exposed Molybdenum Disulfide with N-Doped Carbon Hybridization: A Hierarchical Hollow Electrocatalyst for Carbon Dioxide Reduction

Journal

Advanced Energy Materials, 9(18)

ISSN

1614-6832

Authors

Li, Haoyi
Liu, Xiaozhi
Chen, Shuangming
et al.

Publication Date

2019-05-01

DOI

10.1002/aenm.201900072

Peer reviewed

ADVANCED ENERGY MATERIALS

www.advenergymat.de

Edge-Exposed Molybdenum Disulfide with N-Doped Carbon Hybridization: A Hierarchical Hollow Electrocatalyst for Carbon Dioxide Reduction

Haoyi Li, Xiaozhi Liu, Shuangming Chen, Deren Yang, Qi Zhang, Li Song, Hai Xiao, Qinghua Zhang,* Lin Gu, and Xun Wang**

Electrochemical CO_2 reduction (CO_2RR) is a promising technology to produce value-added fuels and weaken the greenhouse effect. Plenty of efforts are devoted to exploring high-efficiency electrocatalysts to tackle the issues that show poor intrinsic activity, low selectivity for target products, and short-lived durability. Herein, density functional theory calculations are firstly utilized to demonstrate guidelines for design principles of electrocatalyst, maximum exposure of catalytic active sites for MoS_2 edges, and electron transfer from N-doped carbon (NC) to MoS_2 edges. Based on the guidelines, a hierarchical hollow electrocatalyst comprised of edge-exposed 2H MoS_2 hybridized with NC for CO_2RR is constructed. In situ atomic-scale observation for catalyst growth is performed by using a specialized Si/SiN_x nanochip at a continuous temperature-rise period, which reveals the growth mechanism. Abundant exposed edges of MoS_2 provide a large quantity of active centers, which leads to a low onset potential of ≈40 mV and a remarkable CO production rate of 34.31 mA cm^{-2} with 92.68% of Faradaic efficiency at an overpotential of 590 mV. The long-term stability shows negligible degradation for more than 24 h. This work provides fascinating insights into the construction of catalysts for efficient CO_2RR.

1. Introduction

Promotions in explorations of catalysts have been identified as a beneficial approach to revolutionize the development of CO_2 reduction reaction (CO_2RR) technologies, which tackles the long-term issues of global warming and energy supply shortage.[1] Electroreduction of CO_2, an effective way to implement carbon recycling, can produce a variety of value-added products powered by renewable electricity, ranging from monocarbon to multicarbon compounds.[2] However, several fundamental limitations obstruct the development of high-efficiency CO_2RR, including large overpotential, competitive reaction (hydrogen evolution reaction), short-lived stability, and poor electrical conductivity for electron transfer.[3] Therefore, highly active and robust electrocatalysts are indeed imperative to address said issues and thus make CO_2RR become a widely used technology for energy conversion.

Due to considerable activity and low cost, MoS_2 has been regarded as a promising alternative to noble-metal electrocatalysts for hydrogen evolution reaction (HER) from water splitting.[4] But for CO_2RR, HER acts as the competitive reaction to degenerate the conversion from CO_2 to CO as a significant industrial gas feedstock.[5] So, it is fascinating to restrain the activity for HER and enhance the catalytic performance for CO_2RR based on the MoS_2 electrocatalyst model. From the perspective of reaction mechanism of the conversion from CO_2 to CO, the key reaction steps are the formation of intermediate *COOH and its protonation process.[5b,6] According to the density functional theory (DFT) calculation predictions in this work, the edge sites of MoS_2 can facilitate the formation of key intermediate *COOH with lower Gibbs free energy. Thus, the first design principle of electrocatalyst is to expose MoS_2 edges as many as possible.[7] On the other hand, the improvement of electron-gain process is of great importance for CO_2RR, which can decrease the activation barrier and promote the electrocatalytic efficiency.[6,8] N-doped carbon (NC) is inclined to transfer electrons to catalytic sites as a rich-electron material, contributing to the enhancement of electrochemical reaction kinetics.[9] We have found that

H. Li, D. Yang, Q. Zhang, Prof. H. Xiao, Prof. X. Wang
Key Lab of Organic Optoelectronics and Molecular Engineering
Department of Chemistry
Tsinghua University
Beijing 100084, China
E-mail: haixiao@tsinghua.edu.cn; wangxun@mail.tsinghua.edu.cn

X. Liu, Dr. Q. H. Zhang, Dr. L. Gu
Beijing National Laboratory for Condensed Matter Physics
Institute of Physics
Chinese Academy of Sciences
Beijing 100190, China
E-mail: zqh@iphy.ac.cn

X. Liu, Dr. Q. H. Zhang, Dr. L. Gu
School of Physical Sciences
University of Chinese Academy of Sciences
Beijing 100049, China

Dr. S. Chen, Prof. L. Song
National Synchrotron Radiation Laboratory
CAS Center for Excellence in Nanoscience
University of Science and Technology of China
Hefei 230029, China

The ORCID identification number(s) for the author(s) of this article can be found under https://doi.org/10.1002/aenm.201900072.

DOI: 10.1002/aenm.201900072

there is electron transfer from NC to MoS_2 edges during the CO_2RR, further decreasing the Gibbs free energy of intermediate *COOH. Therefore, NC hybridization is another remarkable design principle of electrocatalyst to improve CO_2RR performance.

In this work, we have synthesized a hierarchical hollow catalyst for CO_2RR comprised of NC and edge-exposed 2H MoS_2 (NCMSH) prepared by a zeolitic imidazolate frameworks (ZIF)-assisted method. ZIFs are used for synthetic templates of hollow structures and carbonization at high temperatures for the formation of NC as an electron donor and electrical conductivity promoter.[10] Studies illustrating the observations for the growth process of edge-exposed MoS_2 nanosheets are scarce. This work demonstrates in situ transmission electron microscopy (TEM) observation of the growth process of NCMSH at an atomic scale that was carried out by using a specialized Si/SiN_x nanochip at different controlled heating temperatures based on an in situ TEM holder.[11] Based on this advanced technology, we deduced the growth mechanism of NCMSH. The NCMSH exhibited extremely low onset potential of ≈40 mV, which was much superior compared to that of other transition metal dichalcogenide (TMD) and NC-based electrocatalysts.[7,12] The current density of 34.31 mA cm^{-2} could be achieved at an overpotential of 590 mV with highest selectivity of 92.68% for Faradaic efficiency (FE). The NCMSH displayed remarkably high CO production rates of 31.80 and 30.75 mA cm^{-2} at 590 and 690 mV of overpotentials respectively, which is equivalent to a threefold enhancement of edge-exposed MoS_2 hollow cages (MSH) for CO_2RR efficiency. At meantime, such high current density and selectivity keep stable for more than 24 h with negligible degradation. This investigation provides a fascinating opportunity to explore the intrinsic catalytic characteristic of MoS_2 for CO_2RR, which demonstrates a great achievement of high performance with earth-abundant materials and paves the way for the desirable design of MoS_2-based electrocatalysts for CO_2RR.

2. DFT Calculation Prediction

In order to guide the material design and understand the atomistic origin of the boost in performance for CO_2RR, we studied the underlying mechanisms on different catalyst models with DFT calculations. The following electrochemical steps were considered

$$* + CO_2 + H^+ + e^- \rightarrow *COOH \quad (1)$$

$$*COOH + H^+ + e^- \rightarrow * + CO + H_2O \quad (2)$$

of which the first step was suggested as the potential limiting step (PLS).[8a] **Figure 1**a shows the comparison of calculated free energy profiles for CO_2RR catalyzed by different models (Figure S1, Supporting Information), and MoS_2 @ NC catalyst was predicted to be the best (with an overpotential of 0.46 V) among all models considered. On the basal plane of MoS_2 and NC models, the PLS was indeed the first step, while on the pristine MoS_2 edge and MoS_2 edge @ NC models, the PLS became step 2, in which the *COOH needed to be reduced to recover the original bare Mo site. The predicted improvement of MoS_2 edge @ NC model over the pristine MoS_2 edge could be attributed to the electron donation from the NC support to the surface Mo sites on the exposed edge (Figure 1b). This extra electron density–stabilized regions stand for electron gain, and the turquoise colored regions for holes upon contact between MoS_2 edge and NC, in which the brown colored for the undercoordinated bare surface Mo sites, and thus facilitated the recovery of original active center in step 2, leading to a lower overpotential. N doping in our NC substrate for DFT calculations was deployed as graphitic N that rendered the NC substrate electron-rich, and thus it was expectable that our DFT calculations showed significant electron transfer from the NC substrate to the MoS_2 edge that was electron-deficient (Figure 1b), even though the NC substrate was weakly bound

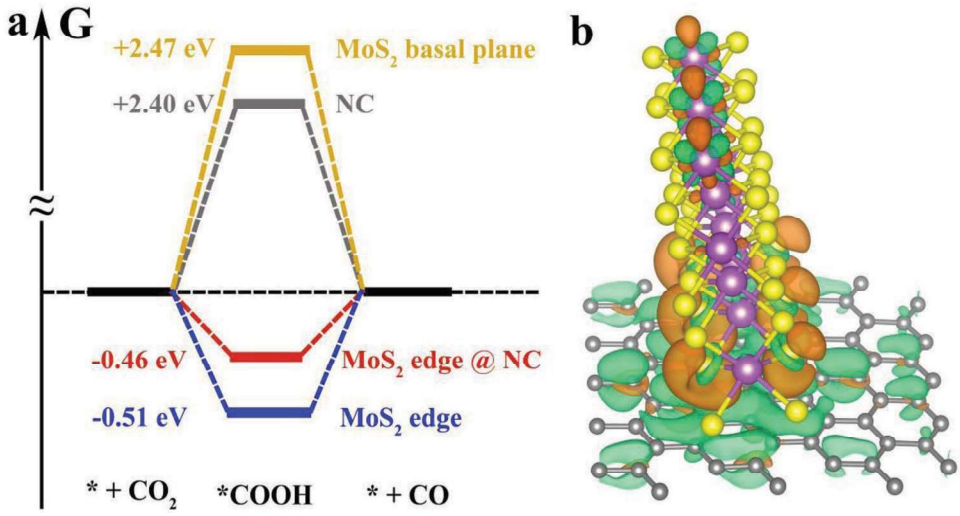

Figure 1. a) The DFT calculations for demonstrating free energy profiles for CO_2RR catalyzed by different models at the equilibrium potential of –0.11 V. b) The illustration of electron density change in the NCMSH model.

to the MoS_2 edge. The electron transfer propagated effectively to the other MoS_2 edge that was far from the NC substrate because of two reasons: 1) any MoS_2 layers in-between the two edges were fully saturated and could not accommodate the extra electrons well; 2) MoS_2 as a semiconductor had poor screening, and thus the electrostatics on one edge could affect the other significantly even with hundreds of layers in-between. A possible reason for the catalytic activity was that the stabilization of surface Mo sites by electron donation from NC resulted in more active edges exposed. Thus, the NC support in MoS_2 edge @ NC catalyst played an essential role as a promoter in boosting the performance for driving CO_2RR.

3. Synthesis and Characterizations of NCMSH

Based on the guidelines from DFT calculations, we have constructed hierarchical hollow cages comprised of NC and edge-exposed 2H MoS_2 for CO_2RR, denoted as NCMSH. The synthetic strategy was illustrated schematically in **Figure 2**. The highly crystallized ZIF-67 generated from Co^{2+} nodes and 2-methyl imidazole (MeIm) ligands was utilized as the template and carbon source for the final product.[10a,c] ZIF-67 displayed uniform and well-defined rhombododecahedral morphology with size distribution from 600 nm to 1 µm (Figure S2a–c, Supporting Information). The crystal structure of ZIF-67 was confirmed by the X-ray diffraction (XRD) pattern in Figure S2d (Supporting Information). In the second step, ZIF-67 and Ni(II) ions were used to prepare a core–shell nanostructures comprised of Ni–Co hydroxide shell and ZIF-67 core (ZIF-67@NiCoH) through the Kirkendall cavitation,[13] which was demonstrated by TEM images, XRD pattern, and energy-dispersive X-ray (EDX) elemental mapping results (Figure S3, Supporting Information). Owing to the excellent reactivity and carrier function of hydroxides, the molybdenum oxysulfide (MoO_xS_y) precursor was then successfully deposited on the Ni–Co hydroxides nanosheets, the shell of ZIF-67@NiCoH, by a solvothermal method, denoted as ZIF-67@NiCoH-MS.[10a,14] The structure and composition of ZIF-67@NiCoH-MS were elucidated in Figure S4 (Supporting Information). Afterward, the hybrid precursor was pyrolyzed at 700 °C in the reductive atmosphere of H_2/Ar (5% of volume fraction). The MeIm ligands were carbonized to NC and the MoO_xS_y precursor was reduced to MoS_2. Co and Ni metal nanoparticles generated from Co nodes and Ni–Co hydroxides were removed by sulfuric acid solution. The NCMSH could be obtained as the final product.

TEM and scanning electron microscopy (SEM) images (**Figure 3**a; Figure S5a–c, Supporting Information) showed that NCMSH maintains the pristine morphology and size distribution of ZIF-67. There were also abundant vesicle-like nanostructures in the hollow cage. When zooming in each single vesicle (Figure 3b), it formed by the curliness of multilayered MoS_2 nanosheets. The interlayer space of 0.63 nm and the lattice planes of (100) with 0.27 nm of lattice space could be characterized by high-resolution TEM (HRTEM), which corresponded to 2H MoS_2 crystal structure (Figure 3b; Figure S5d, Supporting Information). Aberration-corrected high-angle annular dark-field scanning transmission electron microscopy (AC HADDF-STEM) image displayed orderly arranged MoS_2 multilayers with exposed edges and the corresponding crystal models revealed the exposure of terminating Mo edges (Figure 3c). As shown in Figure 3d,e, the curly shape of single-layer MoS_2 nanosheet was captured, which confirmed the formation of vesicle-like nanostructures. The simulated crystal structure demonstrated the typical hexagonal symmetry of 2H MoS_2. The corresponding line scan profile marked in Figure 3e further elucidated Mo atoms as the terminating atoms (Figure 3f). EDX elemental mapping results illustrated uniform distribution of the five elements (Figure 3g). The elemental ratio indicated the stoichiometric ratio of MoS_2 and nitrogen doping phenomenon (Figure S6, Supporting Information). As testified by Brunauer–Emmett–Teller (BET) measurements (Figure S7, Supporting Information), NCMSH possessed larger surface area and more abundant porosity than MSH (Table S1, Supporting Information). Meanwhile, NC was certified to have a positive effect on the enlargement of surface area by making a comparison of the surface area values between NCMSH and MSH. As a result, a large quantity of exposed Mo edges increased the number of active sites for CO_2RR. The porous and hollow nanostructures enlarged the specific surface area and benefited for the gas permeability and electrolyte diffusion.

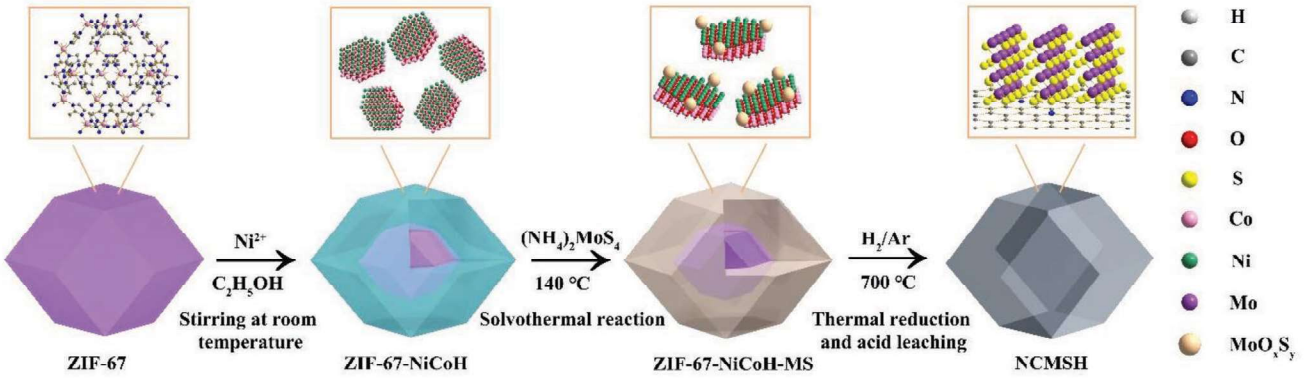

Figure 2. Schematic representation of the synthetic process of NCMSH. The precursor of ZIF-67@NiCoH-MS was obtained through Kirkendall cavitation of Ni(II) ions and subsequent deposition of the MoO_xS_y with a liquid-phase solvothermal strategy. The NCMSH could be generated by a simple thermal annealing and reduction process from ZIF-67@NiCoH-MS at a mixed atmosphere of H_2/Ar (5% of volume fraction) and acid leaching for removing large-size Co- and Ni-based nanoparticles.

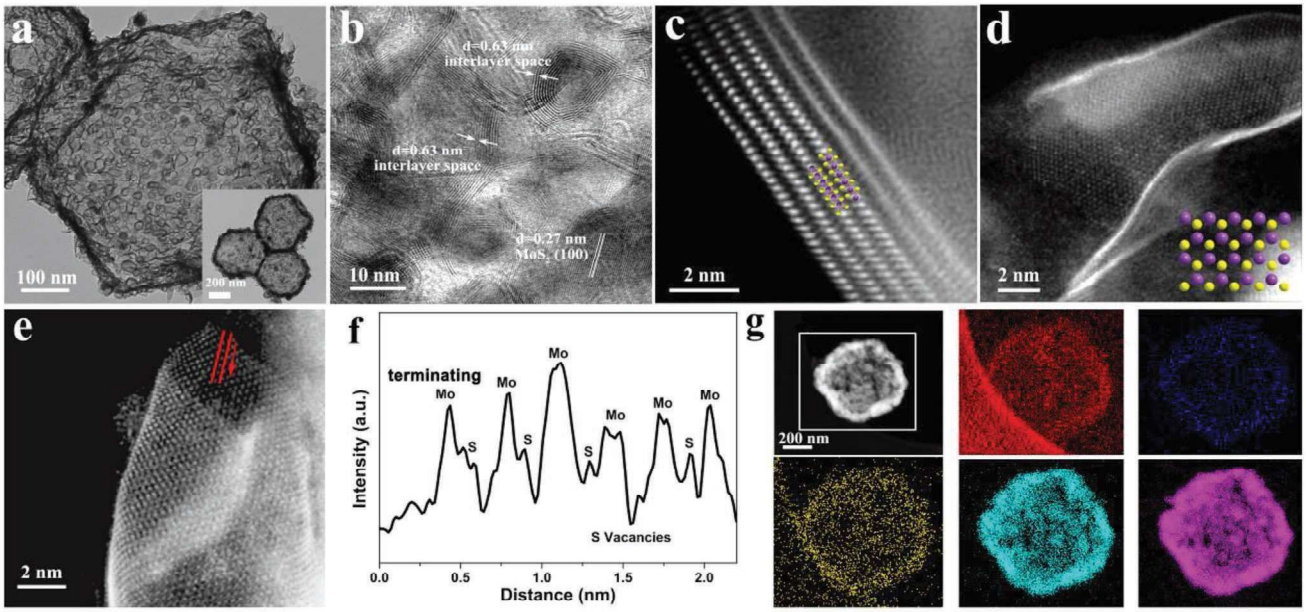

Figure 3. a) TEM, b) HRTEM, c–e) AC HAADF-STEM, and f) corresponding line scan profile marked in (e). g) STEM and EDX mapping results of NCMSH showing uniform distribution of the five elements, C (red), N (blue), O (yellow), Mo (cyan), and S (pink). The inset of (a) exhibits the same shape and size distribution of NCMSH as ZIF-67. The interlayer space of 0.63 nm and lattice distance of 0.27 nm in (b) correspond to the crystal structure of 2H MoS_2. The crystal models in (c) demonstrate the terminating Mo edges of multilayered MoS_2 nanosheets, while the one in (d) shows the typical hexagonal symmetry of 2H MoS_2.

In-depth structural analyses were carried out to investigate the compositions and chemical valence states of NCMSH. The XRD pattern demonstrated that the crystal structure of NCMSH matched well with that of 2H MoS_2 and the characteristic peaks of carbon could not be measured, suggesting the poor crystallinity (**Figure 4**a). The Raman shifts at 381 and 408 cm^{-1} agreed with the E_{2g} and A_{1g} modes of 2H MoS_2, respectively (Figure 4b).[15] The emergence of Raman shifts at 1360 and 1590 cm^{-1} was identified as the D and G bands of carbon material. The high intensity of D band indicated the amorphous feature of carbon in NCMSH, which was corresponding to the XRD results.[16] The synchrotron radiation–based extended X-ray absorption fine structure (EXAFS) was deployed to characterize the local structural details. The X-ray absorption near-edge structure (XANES) spectra and corresponding k^2-weighted FT-R profile at Mo K-edge of NCMSH coincided with that of standard 2H MoS_2, verifying the phase of MoS_2 in NCMSH (Figure 4c,d). The fitting curves and parameters of EXAFS data were summarized in Figure S8 and Table S2 (Supporting Information). The decreased coordination numbers of NCMSH compared to that of 2H MoS_2 foil could be attributed to the existence of vacancies, which further confirmed the results from Figure 3f. X-ray photoelectron spectroscopy (XPS) spectrum (Figure 4e) showed the binding energy of Mo $3d_{5/2}$ and $3d_{3/2}$ located at 229.1 and 232.4 eV, which were the characteristic peaks for 2H MoS_2.[17] Meanwhile, Mo(IV) (229.1 and 233.2 eV) was the dominating state in NCMSH, revealing that MoS_2 was the main product.[4a,18] Moreover, the XPS spectrum of C 1s region further proved the existence of N dopant (Figure 4f).[10a,19] Owing to the low concentration of N in NCMSH, we used synchrotron radiation–based XPS to identify the chemical state of N (Figure S9, Supporting Information). Pyridinic N, graphitic N, and pyrrolic N could be detected and separated, agreeing well with the structure of ZIF-67.[10c]

4. In Situ Observation for Growth Process

We further performed in situ AC HAADF-STEM at expected temperatures to study the growth mechanism of NCMSH. As shown in Figure S10 (Supporting Information), the precursors deposited on a specialized Si/SiN_x nanochip could be calcinated at the expected temperatures and the real-time thermal conduction was achieved by the holder and resistance wires on the chip. At the room temperature, the MoO_xS_y precursors that deposited on the Ni–Co hydroxides exhibited amorphous state and could be regarded as cluster-like compounds (**Figure 5**a). When the chip was heated to 400 °C, Ni–Co hydroxides converted to Ni–Co oxides through dehydration and Ni–Co oxides showed excellent crystallinity with cubic symmetry. In this case, MoO_xS_y still maintained amorphous structures (Figure 5b). Figure 5c revealed MoS_2 nanosheets formed at 600 °C and the edges of MoS_2 (marked by red arrows) gradually appeared under this circumstance. Meanwhile, Ni–Co oxides were reduced to corresponding metals and NC coated the nanocrystals (marked by yellow arrows). Due to the insufficient reduction ability of the vacuum environment in the instrument and the existence of sulfur source from the conversion of MoO_xS_y to MoS_2, Ni–Co oxides could be partially sulfureted to sulfides. Therefore, we could observed Co_9S_8 nanocrystals under this condition.[14b] Since it came to 800 °C,

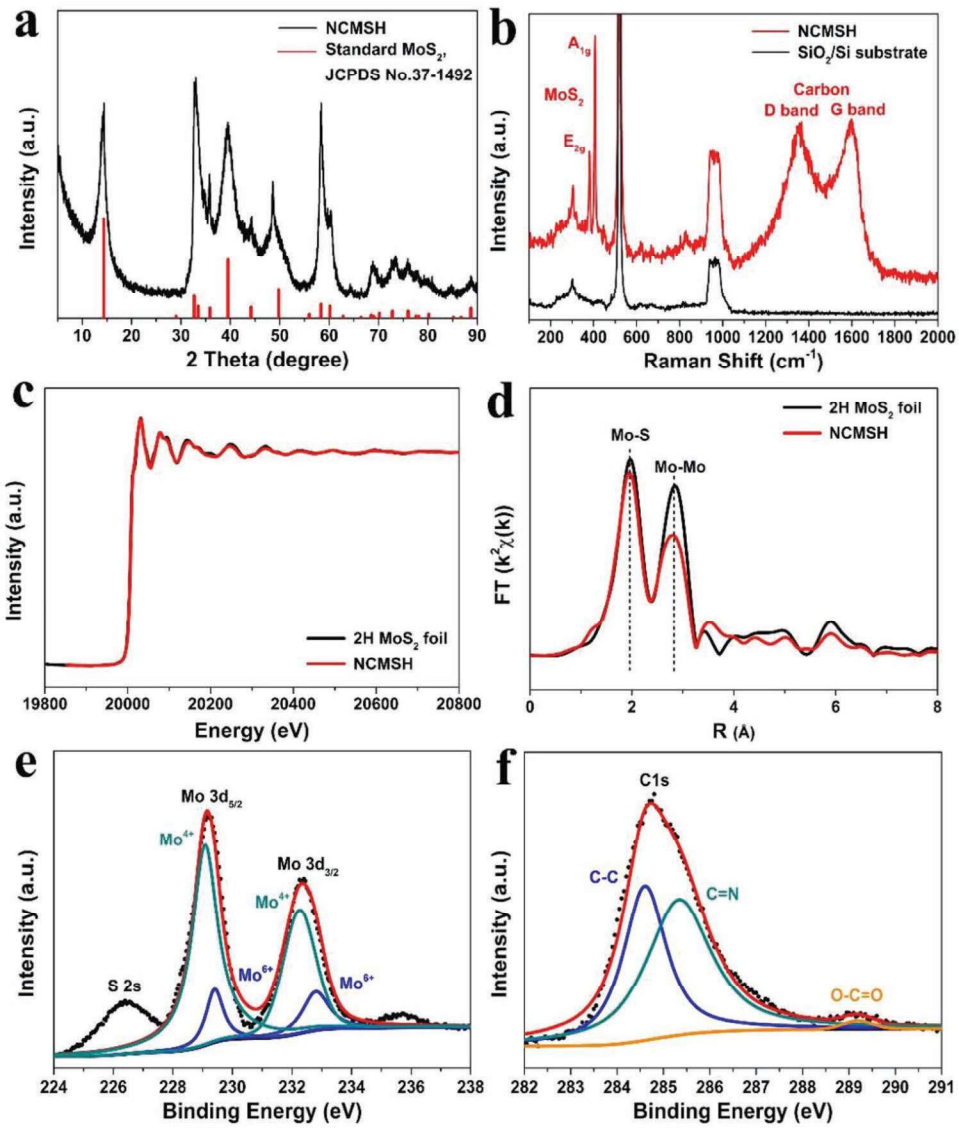

Figure 4. a) XRD pattern, b) Raman spectrum, c,d) Mo K-edge XANES spectra and corresponding k^2-weighted FT-R profile from EXAFS results, and e,f) XPS spectra of Mo 3d and C 1s regions with fitting curves of NSMSH.

it was obvious for the presence of abundant exposed edges of MoS_2, which wrapped the Ni–Co metal and sulfide nanocrystals (Figure 5d). Here the Ni–Co-based nanoparticles acted as the templates for the coating behavior of MoS_2 growth, which contributed to the curliness shape of MoS_2 nanosheets. In this in situ AC HADDF-STEM mode, we could not achieve the removal of Ni–Co based materials by sulfuric acid solution, so Ni–Co based materials seemed to predominate in the products. When washing out the Ni–Co based nanoparticles, it could be obviously observed for the crimp behavior of MoS_2 nanosheets as shown in Figure 3d,e. Compared to products generated at 600 °C, the amount of NC distinctly increased and acted as the carrier for the nanocrystals. As further increasing the temperatures, the tendency to form bulk materials took place and the exposure of MoS_2 edges degenerated (Figure S11, Supporting Information).

5. Evaluation of CO_2RR Performance

The CO_2RR was performed in a H-type three-electrode cell with two compartments separated by a Nafion-115 proton exchange membrane. CO_2 gas was persistently bubbled into the electrolyte of 4 mol% 1-ethyl-3-methylimidazolium tetrafluoroborate (Emim-BF_4) aqueous solution with a rate of 7 mL min^{-1} for saturating electrolyte and quantitative analysis of gas-phase products through the gas chromatograph (GC). The potentials were calibrated to that versus reversible hydrogen electrode (RHE) and all of the potentials in this study were reported versus RHE (Figure S12, Supporting Information). We also employed other electrocatalysts as the contrastive samples, such as MSH (Figure S13, Supporting Information), commercial MoS_2 (CMS) and carbon nanotubes (CNTs) derived from ZIF-67 (Figure S14, Supporting Information). Linear sweep

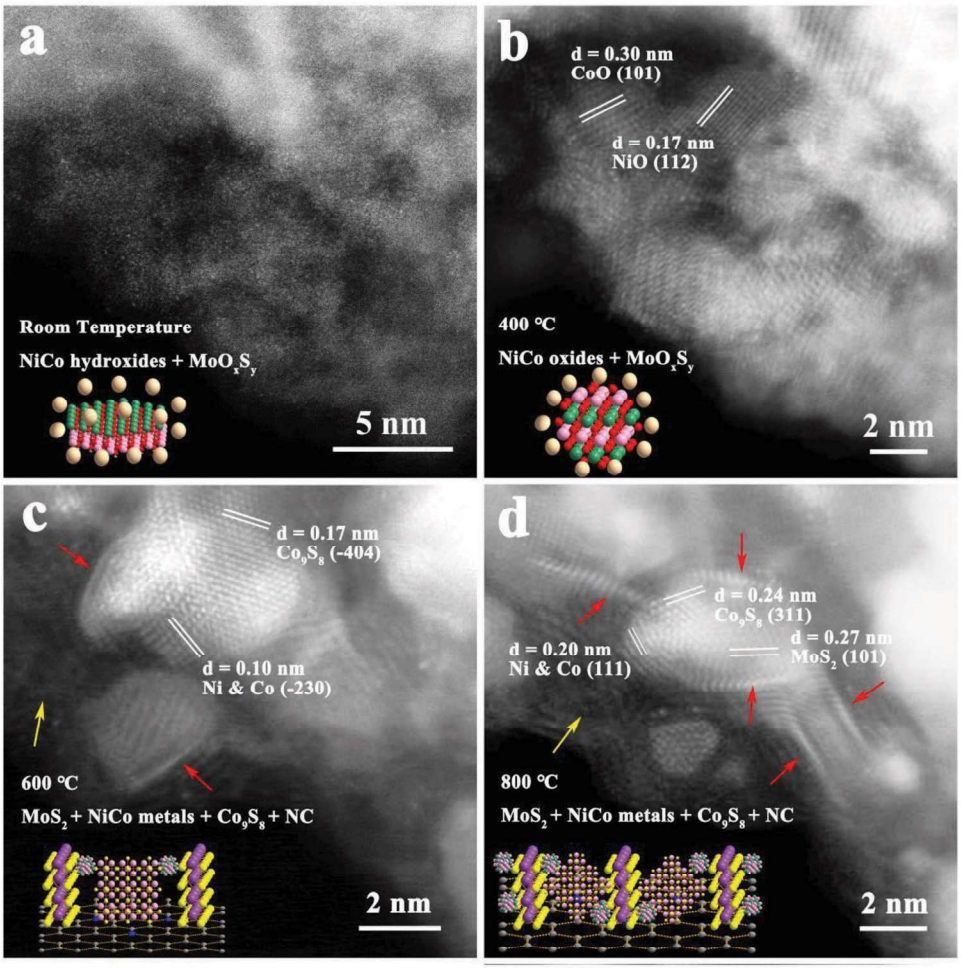

Figure 5. In situ AC HAADF-STEM images of NCMSH captured at a) room temperature, b) 400 °C, c) 600 °C, and d) 800 °C. The insets of crystal structure models show the states of the sample at every temperature stage.

voltammetry (LSV) measurements exhibited the extremely low onset potential of ≈40 mV, which proved the remarkable intrinsic activity of NCMSH (Table S3, Supporting Information). The high current density of 34.31 mA cm^{-2} could be obtained over NCMSH at −0.7 V, which was twofold than that of MSH (**Figure 6**a). The detection results of GC elucidated the products of CO_2RR were H_2 and CO. The Faradaic efficiencies for CO and H_2 production were characterized at different potentials (Figure 6b; Figure S15 and Table S3, Supporting Information). At −0.7 V, NCMSH reach the highest FE of 92.68% for CO production, which was 1.4 times than that of MSH. Meanwhile, the partial current density of CO (Figure S16, Supporting Information) illustrated that both of −0.7 and −0.8 V had remarkable CO production rates of 31.80 and 30.75 mA cm^{-2}, respectively. The comparison of electrocatalytic performances for CO_2 reduction of TMD- and NC-based electrocatalysts were summarized in Table S4 (Supporting Information). The superior performance with high activity and long-term durability of NCMSH could be regarded as an inspiration for the further development of CO_2 electroreduction using TMD materials.

The enhanced activity of NCMSH was attributed to the increased active electrochemical surface area (ECSA), which could be roughly estimated by double layer capacitance (C_{dl}) value (Figure S17, Supporting Information).[20] Such high C_{dl} value of NCMSH was owing to a large quantity of active sites on the exposed edges of MoS_2 (Figure 6c). Meanwhile, the NC hybridization facilitated the enlargement of active sites, which could be further confirmed by BET results (Figure S7, Supporting Information). Because of NC hybridization and carbon fiber paper substrate, superb conductivity of NCMSH promoted the electron transfer during electrocatalysis and thus enhanced the performance, which was testified by Nyquist plots (Figure S18, Supporting Information). Furthermore, NCMSH demonstrated excellent stability for more than 24 h with negligible degradation of the current density and selectivity of CO production (Figure 6d), which was superior compared to that of other samples (Figure S19, Supporting Information). Besides, SEM, TEM, and HRTEM images exhibited the morphological stability of NCMSH (Figure S20, Supporting Information). XRD, XPS, EXAFS spectra (Figures S21 and S22, Supporting Information), and EDX results and corresponding elemental mapping data (Figure S23, Supporting Information) proved the compositional and structural stability of NCMSH during CO_2 electroreduction. The DFT calculations for HER were elucidated

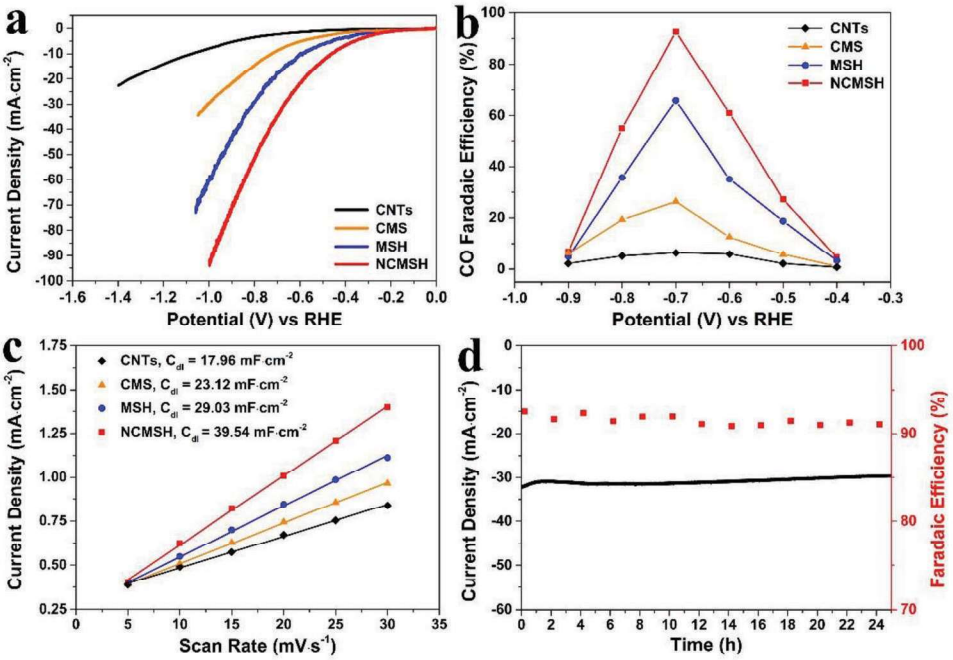

Figure 6. a) LSV curves measured in CO_2-saturated 4 mol% Emim-BF_4 aqueous solution media at a scan rate of 5 mV s^{-1}. b) FEs of CO production. c) C_{dl} measurements. d) Chronoamperometric measurements and corresponding FEs (red points) recorded on NCMSH at a potential of –0.7 V versus RHE.

in Figure S24 (Supporting Information) and the results showed that HER has a lower overpotential than CO_2RR on MoS_2 edge @ NC, which was consistent with our experiments.

We have also carried out the comparative studies on the electrocatalytic performances of CO_2RR for NCMSH with different time of acid leaching, which are expected to demonstrate the impact of remnant Co and Ni parts on CO_2RR performance. As shown in the results of inductively coupled plasma atomic emission spectra (ICP-AES) measurement (Table S5, Supporting Information), different time of acid leaching contributes to different content of Co and Ni in NCMSH samples, which proves that Co- and Ni-based materials still exist in NCMSH and acid leaching cannot remove the whole parts of Co and Ni (Figure S6, Supporting Information). However, excessive Co and Ni (NCMSH without acid leaching) have a negative effect on CO_2RR performance. But for NCMSH with acid leaching, remnant Co and Ni hardly have an influence on the CO_2RR performance of NCMSH given that the contents of Co and Ni in NCMSH change obviously with the increase of acid leaching time, as shown in the polarization curves and Faradaic efficiencies of CO production (Figure S25 and Table S6, Supporting Information).

We further utilized the synchrotron radiation–based XPS and EXAFS spectra to testify the electron transfer process. For the peak positions of Mo 3d regions in XPS spectrum, there is a ≈0.3 eV downshift for NCMSH compared to that of MSH (**Figure 7**a). Besides, about 0.7 eV downshift of pre-edge peak can also be observed in the XANES spectrum at Mo K-edge from EXAFS data of NCMSH compared to that of MSH (Figure 7b). The above downshifts effectively confirmed the electron transfer from NC to MoS_2.[9b,21] For further elucidating the electron transfer process from NC to MoS_2 experimentally, we developed a mechanically mixed nanomaterial of MSH and CNTs for comparisons with NCMSH, MSH, and CNTs. As shown in Figure S26a (Supporting Information), the peak positions of the mixture of MSH and CNTs in XPS spectrum of Mo 3d regions were almost the same as that of MSH, which have an upshift about 0.3 eV compared to that of NCMSH. This result proved that the as-prepared NCMSH was not comprised of mechanically mixed MoS_2 and NC and the two components have the electronic interaction. As for the CO_2RR performance, the mixture showed a little better polarization ability and selectivity of CO production than MSH, but far from that of NCMSH (Figure S26b,c, Supporting Information). However, the reactive resistance of the mixture was quite less than that of MSH, showing similar level as NCMSH and CNTs. Therefore, the influence of NC on NCMSH was not just the enhancement of conductivity, but electron donor more importantly.

We have developed other systems for CO_2RR performance as comparative studies showing superior manner of NCMSH. The NC was changed to reduced graphene oxide (rGO) for hybridizing with MoS_2. As shown in Figure S27a,b (Supporting Information), the hybrid nanostructures of MoS_2 and rGO nanosheets were synthesized by the similar method as NCMSH. The EDX result showed the elemental ratio of Mo and S matches well with the stoichiometric ratio of MoS_2 (Figure S27c, Supporting Information). The Raman spectrum further confirmed the hybrid components of MoS_2 and rGO (Figure S27d, Supporting Information). However, the CO_2RR performance of MoS_2/rGO demonstrated poorer than that of NCMSH and MSH according to the polarization ability and Faradaic efficiencies of CO production (Figure S27e,f, Supporting Information). The electrical conductivity of MoS_2/rGO maintained similar level as that of NCMSH and CNTs, even much better than that of MSH, which indicated that the intrinsic activity of MoS_2/rGO was weaker than that of NCMSH

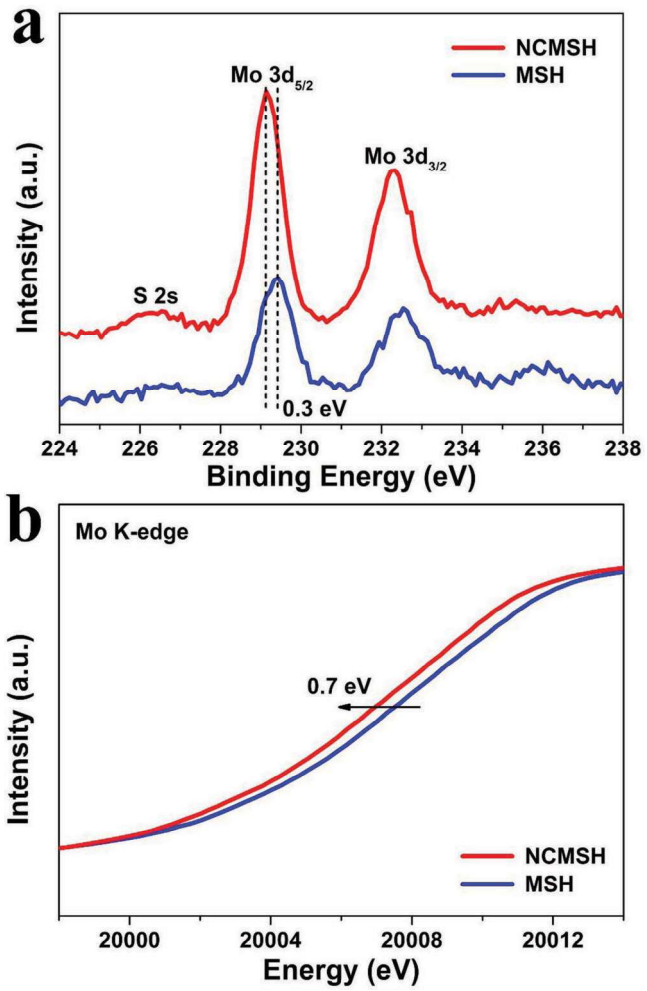

Figure 7. Synchrotron radiation–based a) XPS spectrum of Mo 3d regions for NCMSH and MSH; b) Mo K-edge XANES spectra of NCMSH and MSH from EXAFS results.

and MSH. We have also made a comparison of CO_2RR performance between NCMSH with carbon fiber paper and carbon cloth. Both of the two samples with the same mass loading exhibited excellent electrocatalytic performance. At low current density level, the two samples had almost the same polarization capability but NCMSH with carbon fiber paper slightly dominated at large current density level (Figure S28a, Supporting Information). Meanwhile, the two samples had similar behavior in the selectivity of CO production and reactive resistances (Figure S28b,c, Supporting Information), which indicated that the expanded substrate, carbon cloth, was also efficient for CO_2RR electrocatalysis.

6. Conclusion

In summary, based on the guidelines for performance enhancement from DFT calculations, maximum exposure of catalytic active sites for MoS_2 edges and electron transfer from NC to MoS_2 edges, we have constructed a hierarchical hollow electrocatalyst comprised of edge-exposed 2H MoS_2 hybridized with N-doped carbon by high-temperature pyrolysis and reduction. We utilized systematic material characterization technologies, such as XRD, Raman, EXAFS, and XPS to prove the great achievement of pristine design and construction for composition and structure of the electrocatalyst. Notably, we deployed in situ AC HADDF-STEM to reveal the growth mechanism of NCMSH by using a specialized Si/SiN_x nanochip at expected and controlled heating temperatures. As a result, NCMSH possessed lower onset potential and higher CO production rate and selectivity than that of MSH and CMS which elucidated the superiority of hybrid catalyst. The high intrinsic active and long-term stability of the performance for CO_2RR has made a great progress compared to the previously reported electrocatalysts. Our experimental and theoretical findings created a splendid model for practical applications of CO_2RR and provided guidelines for promoting catalytic activity for target reaction and restrain it for competitive reaction. This electrocatalyst facilitates the development of earth-abundant electrocatalysts based on MoS_2 and other TMD based materials with further promoted electrocatalytic performances.

7. Experimental Section

Synthesis of ZIF-67: ZIF-67 was synthesized via a liquid-phase method as reported previously.[19] In a typical synthesis, 0.291 g $Co(NO_3)_2 \cdot 6H_2O$ was dissolved in 20 mL methanol with ultrasonication to form a homogeneous solution. Then, 0.328 g 2-methyl imidazole (MeIm) was dissolved in 20 mL methanol with ultrasonication to form a homogeneous solution. The two solution was mixed and stirred for 2 min at room temperature. Subsequently, the mixed solution was sealed in an oven at 40 °C for 20 h. The purple precipitates were washed by ethanol several times and centrifuged to obtain solid products. The products were dried at 70 °C in vacuum for 5 h.

Synthesis of NCMSH: First, 0.04 g ZIF-67 powder was dispersed in 25 mL ethanol with ultrasonication to form a homogeneous solution. Then, 0.08 g $Ni(NO_3)_2 \cdot 6H_2O$ was added to the above solution and the mixed solution was stirred for 45 min at the room temperature. After this operation, a core–shell nanostructures formed that was comprised of Ni–Co hydroxide shell and ZIF-67 core (ZIF-67@NiCoH).[10a] The lilac precipitates were centrifuged and subsequently dispersed in 10 mL ethanol with ultrasonication to form a homogeneous solution. Next, 0.008 g $(NH_4)_2MoS_4$ was added to the above solution with stirring to obtain a deeply purple homogeneous solution. The mixed solution was sealed in an autoclave and heated at 140 °C for 4 h. After cooling down naturally, the precipitates were washed by ethanol several times and centrifuged to obtain solid products. The products were dried at 70 °C in vacuum for 5 h. After the above operation, the molybdenum oxysulfides (MoO_xS_y) precursor was successfully deposited on the shell of ZIF-67@NiCoH, denoted as ZIF-67@NiCoH-MS. The ZIF-67-NiCoH-MS in a porcelain boat was placed in a tube furnace and heated to 700 °C (the heating rate was 2 °C min^{-1}) for 3 h in a stream of 5% (volume fraction) mixed gas of H_2/Ar (the flow rate was 20 mL min^{-1}). The products were dispersed in dilute H_2SO_4 aqueous solution (0.5 M) and stirred for 12 h at room temperature to remove the Co and Ni metals in the products. Subsequently, the precipitates were washed by deionized water and ethanol several times and dispersed in ethanol for further characterizations.

Synthesis of MSH: The synthetic method of MSH was the same as that of the NCMSH except that the formation time of ZIF-67@NiCoH prolonged to 2 h and the hollow nanostructures replaced the previous core–shell nanostructures. The target was to remove the ZIF-67 core to eliminate the carbon source.

Synthesis of CNTs: In a typical procedure, ZIF-67 in a porcelain boat was placed in a tube furnace and heated to 700 °C (the heating rate was

2 °C min^{-1}) for 3 h in a stream of 5% mixed gas of H_2/Ar (the flow rate was 20 mL min^{-1}). The products were dispersed in dilute H_2SO_4 aqueous solution (0.5 M) and stirred for 12 h at the room temperature to remove the Co and Ni metals in the products. Subsequently, the precipitates were washed by deionized water and ethanol several times and dispersed in ethanol for further characterizations.

Synthesis of Mixture of MSH and CNTs: The as-prepared MSH and CNTs were mixed with the weight ratio of 1:1 by grinding. Then, the product was dispersed in ethanol and ultrasonicated for 30 min. The sample was washed by ethanol several times and centrifuged. The product was dried at 70 °C in vacuum for further characterization.

Synthesis of MoS_2/rGO: The GO nanosheets were synthesized by a modified Hummers method.[22] 0.02 g GO nanosheets and 0.01 g $(NH_4)_2MoS_4$ were dispersed in 10 mL deionized water forming a homogeneous solution. The above solution was sealed in an autoclave and heated at 140 °C for 4 h. After cooling down naturally, the precipitates were washed by deionized water several times and centrifuged. The products were dried at 70 °C in vacuum for 5 h. The obtained hybrid power was placed in a tube furnace and heated to 700 °C (the heating rate was 2 °C min^{-1}) for 3 h in a stream of 5% (volume fraction) mixed gas of H_2/Ar (the flow rate was 20 mL min^{-1}). The products were washed by deionized water several times and dried in vacuum for further characterization.

Characterizations: Scanning electron microscopy, transmission electron microscopy, high-resolution transmission electron microscopy, and scanning transmission electron microscopy (SEM: Hitachi, SU8010, 10 kV; TEM: Hitachi, H7700, 100 kV; HRTEM and STEM: JEOL, JEM-2010F, 200 kV) were carried out to characterize the morphologies and structures of as-prepared samples. AC HADDF-STEM were performed by JEOL JEM-ARM200CF at 200 kV with double spherical aberration (Cs) correctors (CEOS GmbH, Heidelberg, Germany) and cold field emission gun. Energy-dispersive X-ray and elemental mapping results were obtained by JEOL JEM-2010F at 200 kV. X-ray diffraction patterns were measured by Bruker D8 Advance X-ray diffractometer equipped with Cu Kα radiation (λ = 1.5418 Å). Raman spectra were collected with Horiba–Jobin–Yvon Raman system under 514 nm laser excitation with a power of 2 mW. Brunauer–Emmett–Teller measurements were performed through Quantachrome Autosorb-iQ instrument. X-ray photoelectron spectroscopy was achieved through a PHI Quantera SXM spectrometer with monochromatic Al Kα X-ray sources (1486.6 eV) at 20 mA and 2.0 kV. Co, Ni, and Mo contents in NCMSH samples with different times of acid leaching was performed on a 2RIS Intrepid II XSP ICP-AES instrument system. The synchrotron radiation–based extended X-ray absorption fine structure at Mo K-edge was measured at BL14W1 station in Shanghai Synchrotron Radiation Facility (SSRF). The Mo K-edge XANES data were recorded in a transmission mode. The energy calibration was performed by using a Mo metal foil at Mo K-edge. The obtained data were calculated and processed based on the WinXAS3.1 program.[23] Phase-shift functions and theoretical amplitudes were calculated by the FEFF8.2 code and the parameters of crystal structure of the standard 2H MoS_2 foil.[24] The synchrotron radiation–based XPS measurements were carried out at the beamline 4W9B in Beijing Synchrotron Radiation Facility (BSRF). The X-ray was monochromatized by a double-crystal Si (111) monochromator for BSRF. The energy was calibrated using a gold metal foil.

In Situ Observation Measurements of the Growth of NCMSH: The in situ observation of growth process at an atomic scale was carried out on JEOL JEM-ARM200CF, at 200 kV with double spherical aberration (Cs) correctors (CEOS GmbH, Heidelberg, Germany). The sample was dispersed on a specialized Si/SiN_x nanochip and further loaded on a Lightning D9+ in situ TEM holder produced by DENSsolutions. AC HAADF-STEM images were captured at different temperature points in a continuous heating process. The Si/SiN_x nanochip of in situ TEM device is a commercial product purchased from DENSsolutions, which is specially designed to achieve excellent stability against the thermal drift and the external disturbance. During fabrication, specific mechanical stress has been added in the SiN_x supporting films of the chips in advance. Consequently, when the thermal shock occurs, the films will only swell in the perpendicular direction, thus avoiding the unwanted horizontal drifting. Meanwhile, there is a localized closed loop for temperature feedback that can offer guarantees for the heating process and sample stability as shown in Figure S10c (Supporting Information), where the temperature changes with time accurately. A temperature controller connecting with the TEM holder was deployed for heating process, which was achieved by the closed loop on the nanochip. We operated the temperature controller to realize the heating temperature and time precisely. And the temperature-rise and stability periods are less than 5 s. Furthermore, with the above unique designs, the reported sample drift can be as low as 6 picometer per second as 800 °C; the temperature fluctuation can be less than 1 °C at 1300 °C with the ultimate sample drift in 0.5 nm min^{-1}.

Electrochemical Characterizations: The electrocatalytic measurements were performed at room temperature with a Chenhua CHI660e instrument in an H-type three-electrode cell with two compartments separated by a Nafion-115 proton exchange membrane. In this work, all of the electrocatalytic data were collected in the electrolyte of 4 mol% Emim-BF_4 aqueous solution. Ag/AgCl electrode with saturated KCl–AgCl solution and Pt plate were utilized as the reference and counter electrodes respectively. In this three-electrode configuration, reversible hydrogen electrode calibration was carried out in the H_2-saturated electrolyte using a Pt wire as the working electrode. A single cycle of cyclic voltammetry was recorded at a scan rate of 1 mV s^{-1} and the average value of the two potentials where the current crossed the line of zero value was considered as the potential of the calibration. As a result, E (RHE) = E (Ag/AgCl) + 0.491 V. In a typical preparation of working electrode, 1 mg as-prepared catalyst was mixed with 40 µL ethanol and 40 µL Nafion D-520 dispersion, resulting in a homogeneous ink. The ink was loaded on a piece of carbon fiber paper (or carbon cloth) with the area of 1 × 1cm^2. After dried in vacuum at room temperature overnight, the working electrodes were immersed in the applied electrolyte for 12 h in vacuum to activate the electrode. For electrocatalytic processes, the CO_2 airflow was bubbled into the cell at a rate of 7 mL min^{-1} at room temperature under ambient pressure. Before the measurements, several cycles of cyclic voltammetry were performed to activate and stabilize the working electrode. The polarization curves were characterized in the selected potential ranges at a scan rate of 5 mV s^{-1}. The current density was normalized by the geometric surface area of carbon fiber paper. The 1 h chronoamperometry measurements (i–t) were carried out to collect the gas products for characterization of FEs. For the detection of gas products from CO_2 reduction, 1 mL mixed gas collected from the cell passed through the column of a gas chromatograph (Techcomp GC-7900) and was analyzed quantitatively for the content of gas products for 30 min. A molecular sieve TDX-01 and Al_2O_3 capillary column were equipped in the GC and ultrahigh pure Ar was used as a carrier gas. The gas products were analyzed separately by a thermal conductivity detector for H_2 and CO. Meanwhile, the standard calibration curves for H_2 and CO by detecting standard ultrahigh pure H_2 and CO in the GC were plotted for the quantification of the products. The Nyquist plots of electrochemical impedance spectroscopy (EIS) was surveyed in the frequency range of 10 kHz to 10 mHz at the open circuit voltage. The cyclic voltammetry was carried out to assess electrochemical double-layer capacitance (C_{dl}) at no Faradaic processes six times at six different scan rates (5, 10, 15, 20, 25, and 30 mV s^{-1}). The obtained current densities at the selected potential have the linear relationship with the scan rates and the slopes of fitting curves were considered as the C_{dl}. The stability measurements (i–t) were recorded at a constant applied potential of –0.7 V versus RHE and the corresponding FEs were measured by GC every 2 h.

The Calculation Method of Faradaic Efficiency for CO_2RR: The Faradaic efficiency for CO production was calculated according to the following equation

$$\mathrm{FE}(\%) = \frac{Q_{\mathrm{CO}}}{Q_{\mathrm{total}}} = \frac{n_{\mathrm{CO}} * N * F}{\int_0^t i\,dt} \tag{3}$$

where Q_{CO} is the partial electrical quantity for CO production, Q_{total} is the total electrical quantity, n_{CO} is the molar quantity of CO production (measured by the GC and calculated by the ideal gas law), N is the electron transfer number of CO production (here N is considered as 2), and F is the Faradaic constant, 96485 C mol^{-1}.

DFT Calculation Methods: DFT calculations were performed using the Vienna Ab Initio Simulation Package (VASP),[25] with the projector augmented wave (PAW) method[26] for the core–valence interaction and the plane wave basis sets with a cutoff kinetic energy of 400 eV for the valence electron density. The generalized gradient approximation method with the PBE flavor[27] for the exchange-correlation term was used, and the Brillouin zone was sampled by the Γ point only. The convergence criteria were 1×10^{-5} and 1×10^{-7} eV energy differences for solving for the electronic wave function for structure optimization and vibrational frequency calculations, respectively. All atomic coordinates were converged to within 3×10^{-2} eV Å^{-1} for maximal components of forces. The zero-point energies (ZPE) and enthalpy and entropy contributions to free energies at room temperature (298.15 K) were all included as described elsewhere.[8] More computational details such as vacuum layer and unit cell were shown in the Note of Supporting Information.

Supporting Information

Supporting Information is available from the Wiley Online Library or from the author.

Acknowledgements

H.L. and X.L. contributed equally to this work. This work was supported by Ministry of Science and Technology of the People's Republic of China under Contract Nos. 2017YFA0700101 and 2016YFA0202801, National Natural Science Foundation of China (Grant Nos. 21431003, 21521091, 51522212, 51421002, and 51672307), and the Strategic Priority Research Program of Chinese Academy of Sciences (Grant No. XDB07030200).

Conflict of Interest

The authors declare no conflict of interest.

Keywords

charge transfer, edge-exposed MoS_2, electrochemical CO_2 reduction, in situ STEM, N-doped carbon

Received: January 8, 2019
Revised: February 21, 2019
Published online: March 12, 2019

[1] a) W. Bi, C. Wu, Y. Xie, *ACS Energy Lett.* **2018**, *3*, 624; b) T. Zheng, K. Jiang, H. Wang, *Adv. Mater.* **2018**, *30*, 1802066.
[2] T.-T. Zhuang, Z.-Q. Liang, A. Seifitokaldani, Y. Li, P. De Luna, T. Burdyny, F. Che, F. Meng, Y. Min, R. Quintero-Bermudez, C. T. Dinh, Y. Pang, M. Zhong, B. Zhang, J. Li, P.-N. Chen, X.-L. Zheng, H. Liang, W.-N. Ge, B.-J. Ye, D. Sinton, S.-H. Yu, E. H. Sargent, *Nat. Catal.* **2018**, *1*, 421.
[3] D. D. Zhu, J. L. Liu, S. Z. Qiao, *Adv. Mater.* **2016**, *28*, 3423.
[4] a) Y. Li, H. Wang, L. Xie, Y. Liang, G. Hong, H. Dai, *J. Am. Chem. Soc.* **2011**, *133*, 7296; b) Z. Lu, W. Zhu, X. Yu, H. Zhang, Y. Li, X. Sun, X. Wang, H. Wang, J. Wang, J. Luo, *Adv. Mater.* **2014**, *26*, 2683.
[5] a) L. Zhang, Z.-J. Zhao, T. Wang, J. Gong, *Chem. Soc. Rev.* **2018**, *47*, 5423; b) W. Zhang, Y. Hu, L. Ma, G. Zhu, Y. Wang, X. Xue, R. Chen, S. Yang, Z. Jin, *Adv. Sci.* **2018**, *5*, 1700275.
[6] Z. Sun, T. Ma, H. Tao, Q. Fan, B. Han, *Chem* **2017**, *3*, 560.
[7] a) P. Abbasi, M. Asadi, C. Liu, S. Sharifi-Asl, B. Sayahpour, A. Behranginia, P. Zapol, R. Shahbazian-Yassar, L. A. Curtiss, A. Salehi-Khojin, *ACS Nano* **2017**, *11*, 453; b) M. Asadi, B. Kumar, A. Behranginia, B. A. Rosen, A. Baskin, N. Repnin, D. Pisasale, P. Phillips, W. Zhu, R. Haasch, *Nat. Commun.* **2014**, *5*, 4470.
[8] a) T. Cheng, H. Xiao, W. A. Goddard III, *J. Am. Chem. Soc.* **2016**, *138*, 13802; b) H. Xiao, T. Cheng, W. A. Goddard III, *J. Am. Chem. Soc.* **2017**, *139*, 130.
[9] a) M.-R. Gao, X. Cao, Q. Gao, Y.-F. Xu, Y.-R. Zheng, J. Jiang, S.-H. Yu, *ACS Nano* **2014**, *8*, 3970; b) Q. Liu, Q. Fang, W. Chu, Y. Wan, X. Li, W. Xu, M. Habib, S. Tao, Y. Zhou, D. Liu, T. Xiang, A. Khalil, X. Wu, M. Chhowalla, P. M. Ajayan, L. Song, *Chem. Mater.* **2017**, *29*, 4738.
[10] a) P. He, X. Y. Yu, X. W. D. Lou, *Angew. Chem., Int. Ed.* **2017**, *129*, 3955; b) Y. Pan, R. Lin, Y. Chen, S. Liu, W. Zhu, X. Cao, W. Chen, K. Wu, W.-C. Cheong, Y. Wang, *J. Am. Chem. Soc.* **2018**, *140*, 4218; c) C. Zhao, X. Dai, T. Yao, W. Chen, X. Wang, J. Wang, J. Yang, S. Wei, Y. Wu, Y. Li, *J. Am. Chem. Soc.* **2017**, *139*, 8078.
[11] a) Y. Gong, J. Zhang, L. Jiang, J. A. Shi, Q. Zhang, Z. Yang, D. Zou, J. Wang, X. Yu, R. Xiao, Y. S. Hu, L. Gu, H. Li, L. Chen, *J. Am. Chem. Soc.* **2017**, *139*, 4274; b) Q. Zhang, X. He, J. Shi, N. Lu, H. Li, Q. Yu, Z. Zhang, L. Q. Chen, B. Morris, Q. Xu, P. Yu, L. Gu, K. Jin, C. W. Nan, *Nat. Commun.* **2017**, *8*, 104.
[12] a) M. Asadi, K. Kim, C. Liu, A. V. Addepalli, P. Abbasi, P. Yasaei, P. Phillips, A. Behranginia, J. M. Cerrato, R. Haasch, *Science* **2016**, *353*, 467; b) B. Kumar, M. Asadi, D. Pisasale, S. Sinha-Ray, B. A. Rosen, R. Haasch, J. Abiade, A. L. Yarin, A. Salehi-Khojin, *Nat. Commun.* **2013**, *4*, 2819; c) J. Wu, R. M. Yadav, M. Liu, P. P. Sharma, C. S. Tiwary, L. Ma, X. Zou, X.-D. Zhou, B. I. Yakobson, J. Lou, P. M. Ajayan, *ACS Nano* **2015**, *9*, 5364; d) J. Xu, X. Li, W. Liu, Y. Sun, Z. Ju, T. Yao, C. Wang, H. Ju, J. Zhu, S. Wei, Y. Xie, *Angew. Chem., Int. Ed.* **2017**, *56*, 9121.
[13] H. Tianou, W. Wang, X. Yang, Z. Cao, Q. Kuang, Z. Wang, Z. Shan, M. Jin, Y. Yin, *Nat. Commun.* **2017**, *8*, 1261.
[14] a) H. Hu, B. Guan, B. Xia, X. W. Lou, *J. Am. Chem. Soc.* **2015**, *137*, 5590; b) G. Yilmaz, K. M. Yam, C. Zhang, H. J. Fan, G. W. Ho, *Adv. Mater.* **2017**, *29*, 1606814.
[15] S. Jiménez Sandoval, D. Yang, R. F. Frindt, J. C. Irwin, *Phys. Rev. B* **1991**, *44*, 3955.
[16] L. Xie, H. Wang, C. Jin, X. Wang, L. Jiao, K. Suenaga, H. Dai, *J. Am. Chem. Soc.* **2011**, *133*, 10394.
[17] a) H. Li, X. Jia, Q. Zhang, X. Wang, *Chem* **2018**, *4*, 1510; b) C. Tan, X. Cao, X. J. Wu, Q. He, J. Yang, X. Zhang, J. Chen, W. Zhao, S. Han, G. H. Nam, M. Sindoro, H. Zhang, *Chem. Rev.* **2017**, *117*, 6225.
[18] J. H. Nielsen, L. Bech, K. Nielsen, Y. Tison, K. P. Jørgensen, J. L. Bonde, S. Horch, T. F. Jaramillo, I. Chorkendorff, *Surf. Sci.* **2009**, *603*, 1182.
[19] B. Y. Xia, Y. Yan, N. Li, H. B. Wu, X. W. Lou, X. Wang, *Nat. Energy* **2016**, *1*, 15006.
[20] S. Gao, Y. Lin, X. Jiao, Y. Sun, Q. Luo, W. Zhang, D. Li, J. Yang, Y. Xie, *Nature* **2016**, *529*, 68.
[21] a) V. O. Koroteev, L. G. Bulusheva, I. P. Asanov, E. V. Shlyakhova, D. V. Vyalikh, A. V. Okotrub, *J. Phys. Chem. C* **2011**, *115*, 21199; b) X.-F. Lu, L.-F. Gu, J.-W. Wang, J.-X. Wu, P.-Q. Liao, G.-R. Li, *Adv. Mater.* **2017**, *29*, 1604437; c) C. Wang, H. Daimon, S. Sun,

Nano Lett. **2009**, *9*, 1493; d) M. Tahir, L. Pan, R. Zhang, Y.-C. Wang, G. Shen, I. Aslam, M. A. Qadeer, N. Mahmood, W. Xu, L. Wang, X. Zhang, J.-J. Zou, *ACS Energy Lett.* **2017**, *2*, 2177.
[22] L. J. Cote, F. Kim, J. Huang, *J. Am. Chem. Soc.* **2009**, *131*, 1043.
[23] T. Ressler, *J. Synchrotron Radiat.* **1998**, *5*, 118.
[24] A. L. Ankudinov, B. Ravel, J. J. Rehr, S. D. Conradson, *Phys. Rev. B* **1998**, *58*, 7565.
[25] a) G. Kresse, J. Furthmüller, *Comp. Mater. Sci.* **1996**, *6*, 15; b) G. Kresse, J. Furthmüller, *Phys. Rev. B* **1996**, *54*, 11169.
[26] P. E. Blöchl, *Phys. Rev. B* **1994**, *50*, 17953.
[27] J. P. Perdew, K. Burke, M. Ernzerhof, *Phys. Rev. Lett.* **1996**, *77*, 3865.

